AIAA 2013-0529

Fluidic Control of Transonic Shock-Induced Separation

B. Vukasinovic[*], A. N. Gissen [*], A. Glezer[*], and S. Gogineni[†]

[*]Woodruff School of Mechanical Engineering, Georgia Institute of Technology, Atlanta, GA 30332-0405.
[†] Spectral Energies, 5100 Springfield Street, Suite 301, Dayton, OH 45431.

The feasibility of active flow control approaches in suppression of 'large scale' separated flow unsteadiness resulting from the transonic flow separation over rounded geometry is investigated experimentally. The subsonic upstream flow ($M \approx 0.59$) accelerates over the rounded ramp and terminates at the normal shock that induces the flow separation. Two active flow control approaches are tested, focusing on the shock and the shear layer, respectively. Both control approaches significantly suppress sharp velocity/density gradients in the shear layer proportional to the jets' mass flow rate coefficient, but the underlying mechanisms that lead to such results are different. The former utilizes the control jets upstream from the shock, which virtually shape an 'apparent flow boundary' in their interaction with the outer flow. As a consequence, the outer flow becomes locally slowed down just upstream from the shock formation, which contributes to its weakening. The latter flow control approach utilizes the control jets downstream from the shock, which directly target the flow separation, and only indirectly target the normal shock. Overall, it is argued that the main effect of the second flow control approach is in the enhanced mixing and spreading of the shear layer for a low jets' mass flow rate coefficient, and a combination of the flow separation delay and mixing for the higher jets' mass flow rate coefficient.

Nomenclature

C_m	=	Control mass flow rate coefficient
f_k, $k=1\text{-}4$	=	Characterisctic acoustic frequencies
H	=	Ramp height
M	=	Mach number
p_e	=	Static pressure at the test section end
p_i	=	Static pressure upstream from the test section
p_k, $k=1\text{-}13$	=	Static centerline pressures
R	=	Ramp radius
s	=	Surface coordinate
U	=	Mean streamwise velocity component
V	=	Mean cross-stream velocity component
ζ_z	=	Mean vorticity component

I. Background

Compressibility effects, and, in particular, the appearance of shock waves in transonic and supersonic flows can lead to significant penalties in the performance of external (airframes) and internal (propulsion) aerodynamic systems. Shock wave boundary layer interactions (SWBLIs) have been associated with local, and sometimes global flow separation, and pronounced unsteadiness with significant energy and performance losses (e.g., increase in drag) and undesirable aeroelastic effects.[1–4]

The flow physics of the interactions of shock waves with surface boundary layers has been the subject of extensive investigations since the 40's. The early investigations[5–8] established details of the complex nature of these interactions with laminar and turbulent boundary layers at transonic speeds. The interaction of an incident oblique or normal shock wave (which can be caused by an irregularity in wall shape, such as a corner or a step) results in concomitant alteration of both the velocity distribution within the boundary layer and in the wave pattern in the external flow and is typically accompanied by a local flow separation downstream of the shock (e.g., Adamson and Messiter[9]). In particular, the interactions of shock waves with turbulence can lead to substantial unsteadiness and deformation of the shock while the characteristic velocity, timescales and length scales of turbulence change considerably.[10]

The adverse effects of shock boundary layer interactions have prompted much interest in their mitigation using flow control approaches (e.g., Dolling[11]) with varying degrees of effectiveness. Conventional flow control approaches applied to a variety of situations were reviewed in extensive detail by Pearcey[1], including, relevant to the current study, a section which reviews boundary layer control applied to a half-airfoil or a 'bump'. An updated overview of shock control strategies is provided Delery[2], including passive (use of vortex generators and local changes in surface contour) and active (suction and blowing or bleed at the surface, surface cooling) control. The author noted that some of these techniques can be used to either modify the boundary layer upstream of the shock to increase its "resistance" to separation, or can be applied underneath or immediately downstream of the shock. A comprehensive review of early work on the suction and blowing for controlling shock boundary layer interactions was later presented by Viswanath[3]. Several authors (e.g., Lin[12]) described suppression of shock boundary layer separation by the introduction of streamwise vorticity upstream of the shock using low-profile, sub-boundary layer (ramp and vane) configurations of vortex generators (VGs). Ashill et al.[13] reported simultaneous increase in lift and decrease in drag by placing the VGs upstream of a normal shock on an airfoil in transonic flow. Vortex generators placed upstream from a compression corner were successful in reducing fluctionations associated with shockwave unsteadiness[14]. Other passive methods applied to shock boundary layer interactions, shown to reduce drag, are porous surfaces and slots. These, along with a number of other flow control techniques designed to reduce wave drag, were explored in the EuroShock II project, the results of which were compiled and edited by Stanewsky[15]. Holden and Babinsky[16] showed that both ramp and vane VGs significantly suppressed separation induced by a normal shock within a test section duct at $M = 1.5$. However, the authors noted that the VGs which were placed directly underneath the shock also increased the wave drag. In a recent numerical study, Lee et al.[17] demonstrated suppression of separation induced by a terminating normal shock within a diffuser ($M = 1.3$).

Active flow control approaches based on continuous suction and blowing have also been applied for mitigation of shock-induced separation by modification of the boundary layer upstream of the shock. Krogmann et al.[18] demonstrated that high-aspect ratio suction upstream of a normal shock over an airfoil in transonic flow ($M = 0.78$) at off-design conditions led to reduction in the boundary layer thickness and improved the overall aerodynamic performance by delaying the rapid growth of the separation bubble and stabilizing of the shock. These authors noted that even the inactive suction slots (and underlying cavity) had significant beneficial effects in terms of reduction in separation and buffeting ostensibly due to coupled cavity oscillations. Souverein and Debieve[19] used a spanwise array of sub-mm, continuous jets for generation of streamwise vorticity for suppression of boundary layer separation induced by an oblique-shock on a test surface at $M = 2.3$, and noted that the reduction in the characteristic scale of the separation bubble was accompanied by an increase in the frequency of the energetic spectral components of the reflected shock.

More recently, the effectiveness of newer flow control technologies for mitigation of shock boundary layer interactions has been investigated. Kalra et al.[20,21] conducted numerical and experimental studies of magneto-gasdynamic plasma actuators where directional (streamwise-oriented) plasma actuation is effected by a magnetic field. They reported reduction in the separated region with best results when the plasma actuator was positioned at the shock impingement zone. Another approach for controlling an oblique shock was presented by Narayanaswamy et al.[22], who used a thermally driven synthetic jet (using electric discharge) to lock the shock-wave oscillations to the jet pulsating frequency (about 2 kHz) indicating potential for shock stabilization at higher actuation frequencies.

The main emphasis of the current investigation is placed on feasibility of active flow control approaches in suppression of the flow 'large scale' unsteadiness downstream of the shock-induced flow separation under the transonic flow regime. The aerodynamic aspects of both baseline and controlled flows are characterized over a rounded ramp nominal geometry.

II. Experimental Setup and Diagnostics

All the experiments were performed in a small, open-return pull-down high-speed subsonic wind tunnel (test sections speeds of up to $M \approx 0.74$), driven by a 150 HP blower. The schematic of the test section is shown in Figure 1. The modular test section measures $12.7 \times 12.7 \times 61$ cm, and the temperature of the return air is controlled using a chiller coupled with an ultra-low pressure drop heat exchanger. Two static pressure ports and a temperature probe are integrated into the tunnel wall for calibration and monitoring purposes. The first pressure port p_i and the temperature sensor are positioned immediately downstream from the tunnel inlet contraction, upstream from the test section. The second pressure port p_e is placed just upstream from the test section exit plane (Figure 1a). The upper, nominally flat, wall of the test section is fitted with a gradual ramp that terminates as quarter of a cylinder having a radius of $R = H = 20$ mm (Figure 1b). This aft geometry is selected as a generic convex surface that induces a

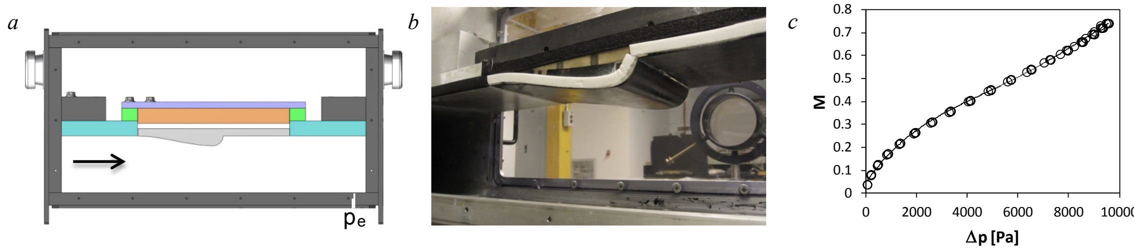

Figure 1. *Schematics of the Georgia Tech test section (a), picture of the profiled top wall (b), and the test section calibration (c).*

localized shock formation in transonic flow conditions, and is adequate for studying the flow dynamics related to the separated flows due to the boundary layer separation in adverse pressure gradient, and due to the shock-boundary layer interaction. The test section having a nominal square cross section is calibrated using a Pitot probe at the center of the inlet cross section. The calibration is done relative to the pressure drop across the inlet contraction ($\Delta p = p_i$), and the resulting calibration curve is shown in Figure 1c.

The flow over the test geometry was first characterized by the upstream (p_i) and downstream (p_e) pressure measurements over a full range of the tunnel speeds (i.e., blower RPMs). The resulting pressure drops over measurement sets of different speed resolutions are shown in Figure 2. As the tunnel speed increases with RPM, both pressure drops increase accordingly, up to the point when the upstream pressure begins to level, which indicates the test section choking point. Inset subplots in each of the plots emphasize this transition from the pre-choked to the choked flow state. After the flow becomes choked, at about 3,200 RPM, the upstream pressure becomes invariant, and that point represents the upper cut-off for the tunnel calibration. As the mass flow rate is invariant in the choked flow regime, further increase in RPM results only in further lowering of the back pressure, illustrated in Figure 2b. Consequently, calibrated upstream Mach numbers are used as reference parameters in the pre-choked flows and downstream pressures p_e are used for reference in the choked flows. Based on these characterizations, two operating conditions were selected for further testing, each representing one of the two nominal regimes: pre-choked and choked. The former was selected such that it results in the strongest pre-choked local shock, at 3,100 RPM. The latter was selected after the choked condition is well established at 3,400 RPM. All the following tests were conducted at both of these transonic conditions, although it should be noted that the pre-choked flow condition should be more relevant to an equivalent airborne platform.

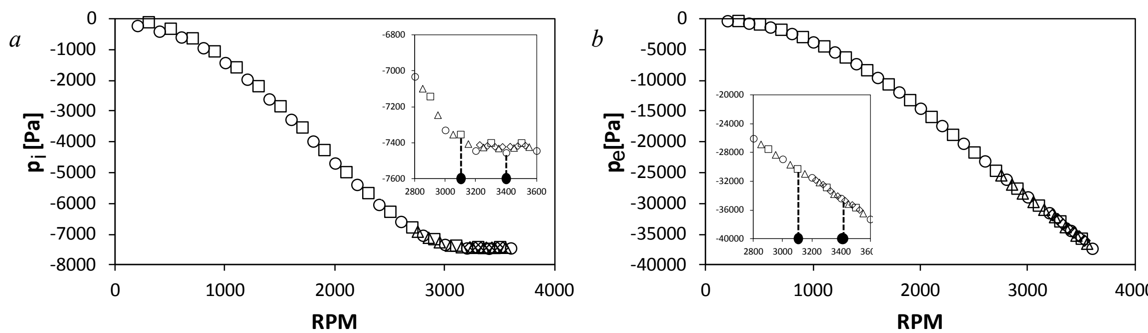

Figure 2. *Characterization of the tunnel flow over nominal ramp geometry: a) pressure p_i downstream from the inlet contraction and b) pressure p_e at the test section end with tunnel RPM. Inset plots emphasize the tunnel choking condition.*

A detailed layout of the 2-D test geometry, along with integrated diagnostic components, is shown in Figure 3. The model is composed of three sections, such that the first one consists of part of the ramp, the second is the main interchangeable section that can have the control devices built into it, and the third one represents the downstream wall. All of the model sections integrate into the upper wall of the tunnel test section. Each main interchangeable section has thirteen static pressure ports distributed along the model centerline (p_1–p_{13}). In addition, an electret condenser microphone was flush mounted into the flat-wall section at L = 10 mm downstream from the control insert. The microphone was used to extract relevant acoustic frequencies under different operating regimes, and to assess the effect of the flow control on these dominant frequencies.

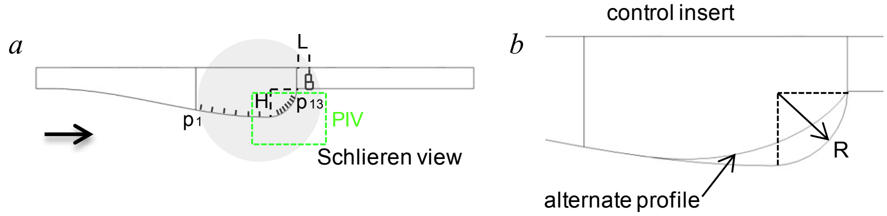

Figure 3. *Schematics of a 2-D model (a), and nominal and alternate surface profile of the control insert.*

Figure 3b emphasizes the curvature of a nominal quarter-circle profile of the control insert aft section. Although assessing its full dependence is outside of the scope of the present study, it is argued that the resulting shock dynamics would be dependent on the actual surface curvature due to the altered pressure gradients and a lack of a surface anchor for the shock. In an ad-hock test of the surface curvature effect, an additional central section for the model profile is designed and tested, having a reduced curvature, as shown as an alternate profile in Figure 3b.

The baseline and controlled flow fields are characterized by planar high-speed PIV measurements (field of view shown in Figure 3a), where each set of data is recorded at 1,000 fps. The mean flow fields and the corresponding statistics of the fluctuating velocity components are based on ensemble averages of 2,000 image pairs. For convenience, all PIV flow fields are shown in an inverted view.

Lastly, the tested flows were characterized by schlieren visualization, where its field of view is centered about the aft section of the ramp, as schematically shown in Figure 3a. Figure 4 shows a double-pass schlieren setup that adapted a PIV-imaging system, having a capability of an image exposure time down to 1 μs. The continuous light-source imposed a lower exposure limit to 200 μs, which is not sufficient to adequately capture small-scale density variations associated with a small-scale turbulence, but it is sufficient for capturing the shock and shock-induced separation features of the flow. In order to enhance quality of schlieren imaging, circular glass sub-windows are integrated into the side-windows of the test section for better optical access.

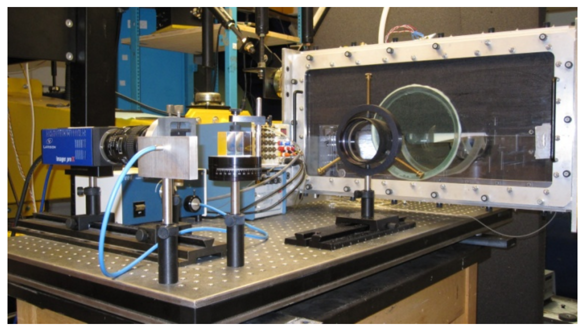

Figure 4. *A double-pass schlieren setup.*

III. Baseline Flow

Global characteristics of the baseline flow are illustrated in a series of schlieren images shown in Figure 5. Prior to formation of the normal shock over the geometry apex, the flow filed exhibits only a sharp density gradient over the incipient shear layer of the separating flow in the adverse pressure gradient, as seen in Figure 5a, which image is taken at M = 0.56, immediately prior the formation of a visible shock. This image also suggests that the flow separates off the ramp just downstream from its apex. Significant pressure/density variations upstream from the ramp apex are observed as the upstream Mach number is increased, as the first highly unsteady weak shock is observed at about M = 0.57 (Figure 5b). This local density gradient is initially weak and unstable, but, with a steady increase in the upstream Mach number (Figures 5c–e), it gradually gains in strength (marked by an increase in density gradient), localizes about the ramp apex, and extends further outward, towards the opposite wall. Nonetheless, the shock appears to be highly unsteady and oscillates in all instances, although the temporal resolution of the schlieren imaging is not sufficient to capture its oscillation frequency. Initial formation of the shock appears to only slightly shift the flow separation upstream (compare Figures 5d and a), as the subsonic separation location is just downstream from the apex. Furthermore, a notable oscillation of the incipient shear layer is observed as well. Figure 5e depicts the pre-choked flow condition that is selected as representative for the pre-choked flow studies, as already described in connection with Figure 2. As the upstream Mach number is further increased, the shock extends to the opposite test section wall, rendering the tunnel flow choked, which state is shown in Figure 5f. It is notable that the shock also begins to tilt slightly forward, which becomes increasingly prominent with further increase of the blower speed. As already stated, the flow mass rate does not change in the choked regime (Figures 5g–j), and further increase in the blower rate only lowers the tunnel pressure downstream from the shock. In response, the shock's forward tilt increases accordingly. Moreover, the shock location also shifts somewhat downstream, over the cylindrical surface. As a consequence, the flow incipient separation, driven by the shock, also

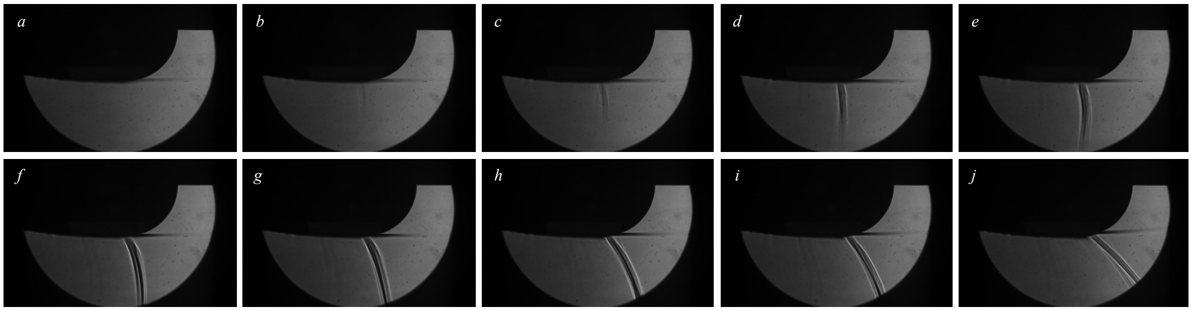

__Figure 5.__ Schlieren visualization of the pre-chocked flow at M = 0.56 (a), 0.57 (b), 0.58 (c), 0.585 (d), 0.59 (e), and 0.592 (f), and the chocked flow with decreasing backpressure from g–j.

shifts downstream (e.g., compare the shear layer origination in Figures 5e and j), and the onset of the baseline flow separation is therefore pushed further downstream than compared to the subsonic separation (Figure 5a).

Three characteristic baseline mean flow fields are shown in Figure 6 in terms of the mean cross-stream velocity component V. The flow approach over the ramp is marked by small positive V component. Prior to the shock formation (M = 0.56, Figure 6a) the flow separates off the short step above the control jets. The V velocity component changes its sign over the apex, which is just upstream from the jets' step, marked by additional dip in V magnitude near the surface. Once the flow separates due to the strong adverse pressure gradient, the evolving shear layer is marked by entrainment from the high speed side (negative V) and from the separated region below (positive V). As the Mach number is further increased, the shock begins to form over the apex. Due to its unsteady nature, the shock-induced discontinuity in the flow field becomes smeared in an ensemble average. Still, even for the pre-choked flow condition at M = 0.59 (Figure 6b), a dividing line of the lowered V is notable right at the apex and upstream from the control jets. Compared to M = 0.56 baseline flow, the flow begins to separate at about the same location on the surface, entrainment into the shear layer intensifies from both sides, and a mark of increased recirculation in the separated flow is visible near the aft surface. Figure 6c depicts the choked flow regime that corresponds to Figure 5h. A sharper discontinuity in V is measured in the averaged flow field, pointing to the shock position at the actuator location ($x/H = y/H = 0$). Further increase in the shear layer entrainment is seen, as well as much stronger recirculation near the aft surface in the separated flow.

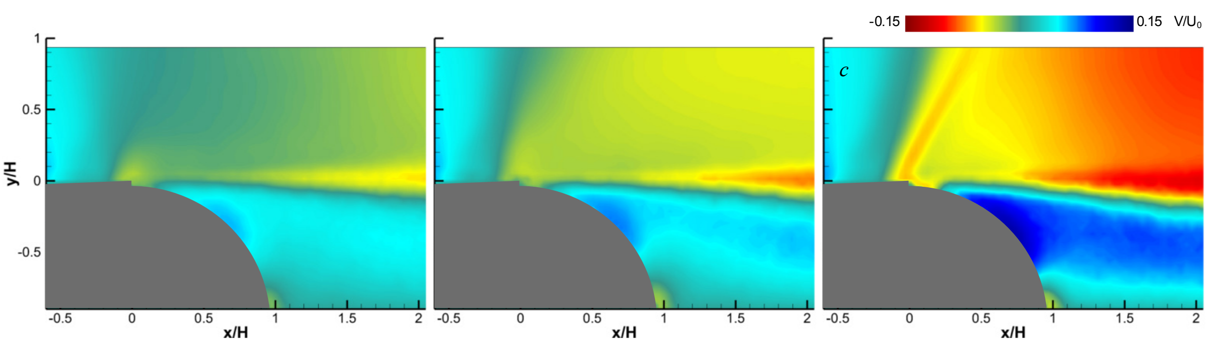

__Figure 6.__ Raster plot of the mean cross-stream velocity component for the baseline flows at M = 0.56 (a) and 0.59 (b), and the choked flow shown in Fig. 5h (c).

Analysis of the acoustic signal measured by the microphone is utilized predominantly to assess the dominant acoustic frequencies in the flow and to relate them to the flow dynamics. Several characteristic examples of the sound pressure power spectra are shown in Figure 7, as the flow over the ramp is driven from subsonic to the pre-choked and choked states. First, each spectrum captures the frequency of the order of 100 Hz, which is related to the blower frequency. The acoustic oscillations prior to the shock formation indicate multiple peaks between about 1 and 2.5 kHz, which are indicated in Figure 7a by its low and high bounds, f_1 and f_2, respectively. As the tunnel speed is increased and pressure/density fluctuations increase upstream from the ramp apex, the high-end frequency peak (f_2,) becomes stronger and dominates the spectrum (Figures 7b and c). However, along with the appearance and strengthening of the normal shock in the pre-choked regime, both f_1 and f_2 become suppressed and broaden, up to the point that only broad remnants of these two peaks are observed at M = 0.59. However, once the flow transitions into the choked regime, two broad, but distinguished peaks are re-established, which are labeled as another pair of representative frequencies f_3 and f_4 in Figure 7f.

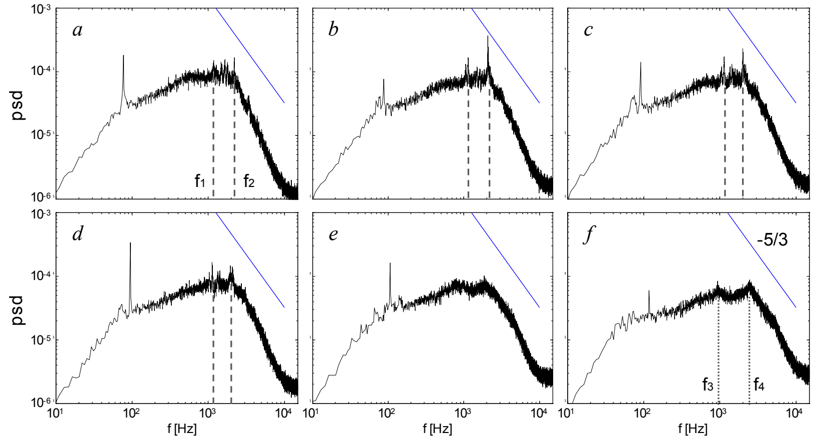

Figure 7. *Power spectra of the measured sound signal at M = 0.49 (a), 0.54 (b), 0.56 (c), 0.57 (d), 0.59 (e), and for the chocked flow shown in Fig. 5h (f).*

Further analysis of the dominant frequencies in the acoustic spectra is shown in Figure 8, where evolution of each of the characteristic frequencies f_1–f_4 is plotted as a function of the upstream Mach number (Figure 8a) up to the choked flow, and as a function of the downstream pressure p_e (Figure 8b), for the choked flow. Several interesting features of the dominant frequencies can be observed. First, both f_1 and f_2 weakly decrease with an increase in M, where the frequency decrease is more pronounced for f_2. Furthermore, as the shock is formed in the pre-choked regime (grayed area in Figure 8a), both frequency evolutions exhibit discontinuous change in slope, along with significant suppression of energy of each peak (as already shown in Figure 7e). The discontinuous drop is more pronounced for the dominant frequency f_1, which could be related to the boundary layer thickening at the shock formation, which would in turn lower the shear layer dominant frequency. Therefore, it is possible that the first dominant frequency is related to the dominant shear layer frequency. The second dominant frequency f_2 becomes significantly amplified at the point of formation of strong pressure/density fluctuations associated with initial compression waves as precursors to the shock formation (see Figures 7b and c), but it is afterwards suppressed and broadened just like f_1, once the shock is fully established. This frequency therefore could be associated with the dynamics of the shock formation. It is interesting to note that the flow in the fully established pre-choked regime does not exhibit any sharp acoustic features, which may also point to variations in shock oscillation across the test span, possibly further accentuated by the end-wall effects. As pointed out with regard to Figure 7, after the dominant frequencies f_1 and f_2 become virtually fully suppressed in the pre-choked regime, two somewhat different, although rather broad dominant frequencies emerge in the choked regime, f_3 and f_4. Besides the fact that f_3 emerges as somewhat lower than f_1, and f_4 higher than f_2, both of them also increase in a similar fashion with a decrease in the back pressure (Figure 8b).

Besides the schlieren flow visualization and acoustic measurements, additional baseline flow characterization was done by the static pressure measurements along the model centerline. A dedicated computer-controlled Scanivalve pressure scanner was used for the pressure measurements. Two sets of pressure ports are distributed upstream and downstream from the model apex, having a gap within a region that would be populated by the flow control elements (Figure 3a). The pressure ports' coordinates are defined as surface coordinates that originate at intersection between the quarter-cylinder and the downstream flat wall (s = 0), and they are normalized by $R = H =$ 20 mm. The pressure ports' negative coordinates indicate their upstream position relative to s = 0.

Figure 9 shows the measured surface pressure profiles for the varying tunnel speeds, where the wall apex is marked by a dashed line for reference. Several noteworthy features should be emphasized. First, it is clear that the region immediately upstream and downstream from the shock is not covered by pressure ports, as the array of upstream pressure profiles indicates a typical evolution over a mildly converging surface, while the

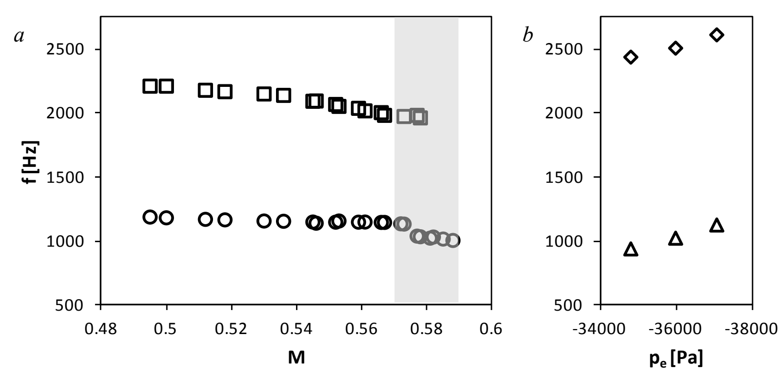

Figure 8. *Evolution of the dominant frequencies in the sound spectra for the pre-chocked (a) and chocked (b) flow: f_1 (○), f_2 (□), f_3 (Δ), and f_4 (◊).*

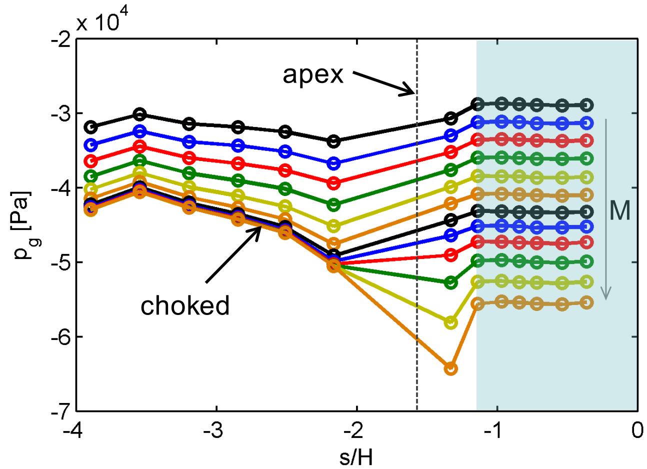

Figure 9. *Surface static pressure profiles with upstream Mach number.*

downstream array indicates that the flow is fully separated at the second downstream port of that array, regardless of the Mach number. The second notable feature is that the pressure profiles also indicate that the flow becomes choked at higher Mach numbers, as all of the upstream pressure profiles virtually collapse onto the same curve. This is additional indication that the two flow regimes are realized in the test section: (i) pre-choked and (ii) choked flow, in accord with the schlieren visualization. All of the following flow control strategies are tested in both of these tunnel flow regimes, although the pre-choked flow regime is considered of a primary interest for the studied problem.

IV. Controlled Flow

As the primary motivation of this investigation is suppression of large-scale unsteadiness of the nominally separated flow coupled to the transonic shock, two control approaches were proposed: (i) active pre-shocking of the flow upstream from the main shock and (ii) suppression of strong velocity/density gradients in the shear layer upon incipient flow separation (Figure 10). The former builds on a well-known passive pre-shocking of the flow, typically in supersonic regimes, and thereby weakening of the primary shock. It is proposed that an active flow control source is utilized instead of typical passive surface ‘obstacles’ that are used in the supersonic flows. The atter approach is motivated by placing the control focus on the resulting shock-induced separation and its mitigation, rather than direct control of its source – a normal shock. Both control approaches utilize active control components that can be addressed on demand.

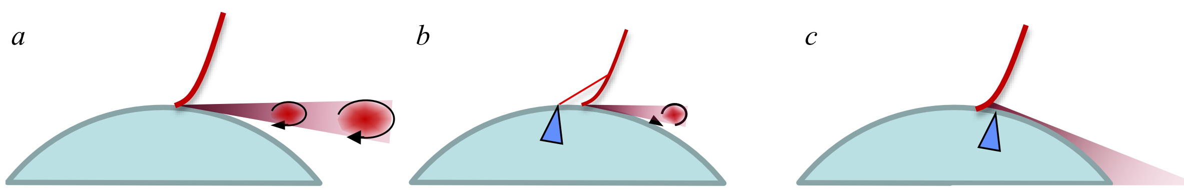

Figure 10. *Schematics of the transonic shock-induced flow separation (a), and the upstream (b) and downstream (c) active flow control approaches.*

Instead of passive control devices typically used in propulsion applications, the present work utilizes their fluidic counterparts, fluidic oscillating jets. These fluidic oscillating jets combine the benefits of unsteady flow control due to their oscillating nature and a net added mass and momentum to the flow, which assist in Coanda effect over the curved surface. Seventeen such fluidic oscillating jets are equidistantly distributed across the model span. Each jet orifice is 1.5 × 1.5 mm and neighboring jets are spaced 7.5 mm apart. In the case of the active shock weakening approach, such array of fluidic oscillating jets is positioned upstream from the ramp apex, i.e., upstream from the transonic shock formation. The jets’ exit orifices are oriented normal to the oncoming flow. The resulting flow effects are tested for three jets’ mass flow rate coefficients $C_m \times 10^3 = 0.6$, 1.7, and 2.6, for both the pre-choked and the choked flow regimes, where C_m is defined as the ratio between the total mass flow rate through the jets and the mass flow rate through the test section.

Figure 11 shows both the schlieren visualization and static pressure profiles for the pre-choked flow regime at $M = 0.59$. It is interesting to note that even a presence of the jet orifices on the surface is sufficient to introduce a compression wave that interacts with the normal shock and presumably weakens it somewhat (Figure 11a, $C_m = 0$). The corresponding pressure profile (Figure 11b) indicates a steeper pressure drop upstream from the jet orifices and upstream from the apex, and a typical indication of the flow separation downstream. Once the flow control is applied, the jet interaction with the primary shock appears to weaken the primary shock, and, even more so, to

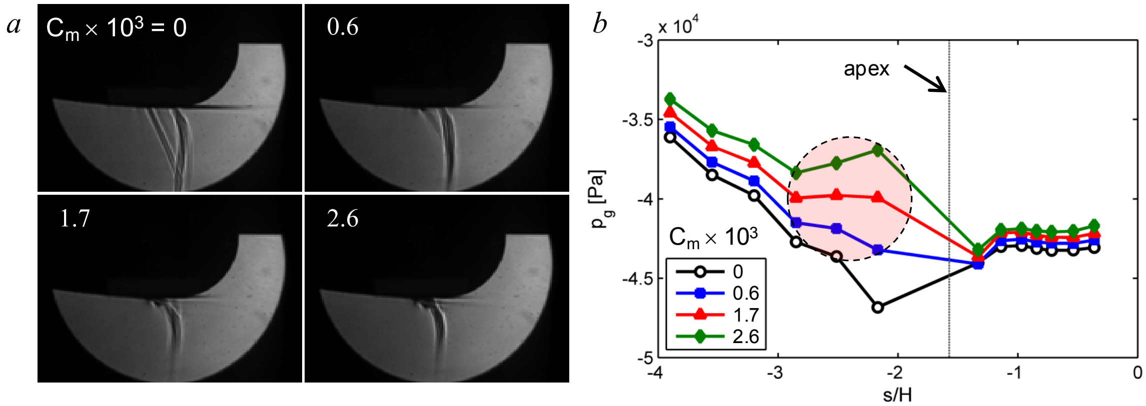

Figure 11. *Shock control in the pre-choked flow (M = 0.59) at four C_m: a) Schlieren visualization and b) surface static pressure profiles. .*

suppress sharp density gradients in the shear layer, as they progressively diminish with an increase in C_m (Figure 11a), most likey due to the introduction, by the fluidic oscillators, of small scale fluctuations and enhanced mixing The accompanying pressure profiles (Figure 11b) indicate that there is an uncompensated increase in losses with an increase in C_m, as the family of pressure curves shifts upward, but more importantly, there is an apparent change in a shape of the pressure profiles upstream from the apex. These profiles indicate that there is a pressure increase upstream from the apex (shock) due to the flow control jets, as the interaction bubble of the control jets and the oncoming flow induce an altered "boundary" to the outer flow and virtually shapes an 'apparent flow boundary'. As a consequence, the outer flow becomes locally slowed down just upstream from the shock, which contributes to its weakening.

The corresponding spectra of the sound pressure fluctuations are shown in Figure 12 for the baseline and controlled flows examined in Figure 11. First, it is interesting to note that the baseline spectrum is not fully featureless, as the two dominant frequencies f_1 and f_2 are still present, with f_3 emerged, although significantly broadened. Once the control jets were activated, there is a clear shift with respect to the baseline case, where energy of sound pressure decreases for low frequencies, up to about 1 kHz, and not much difference is registered in this suppression among the three control cases. On the other hand, energy of high-frequency pressure somewhat increases proportionally with the jets' flow rate. It is also noted that none of the spectral peak of the baseline flow becomes fully suppressed under the controlled flow condition.

Figure 13 shows the results analogous to data shown in Figure 11, only for the choked flow regime. Note that, although both pre-choked and choked shocks originate at about the same location on the surface, once the flow becomes choked, there is a marked increase in shock wave incidence angle. This change also appears to shift the flow separation slightly downstream, but both shear layers seem to show similar levels of density gradients (compare Figures 11a and 13a, $C_\mathrm{m} = 0$). It is also seen that as the shock becomes tilted in the choked regime, the compression waves emanating from the jet orifices do not directly interfere with it, as it is the case in the pre-choked regime. Aside from minor differences, all major features of the controlled cases are analogous, and it can be argued that the 'virtual boundary shaping' by the control jets is robust enough to effect the similar level of control even in the choked flow conditions, only at the somewhat weaker level, as evidenced by somewhat stronger remnants of the shear layer density gradients (compare Figures 13a and 11a). It should be also noted that, as the jets are operated at the given mass flow rate for both regimes, the actual control mass ratio is lower for the choked than for the pre-choked regime, which also contributes to somewhat weaker effect in the former.

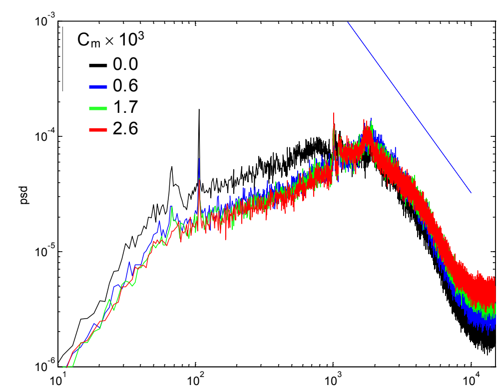

Figure 12. *Power spectra of the sound pressure for the baseline (C_m = 0) and controlled flows with varying C_m for the flow conditions equivalent to Fig. 11.*

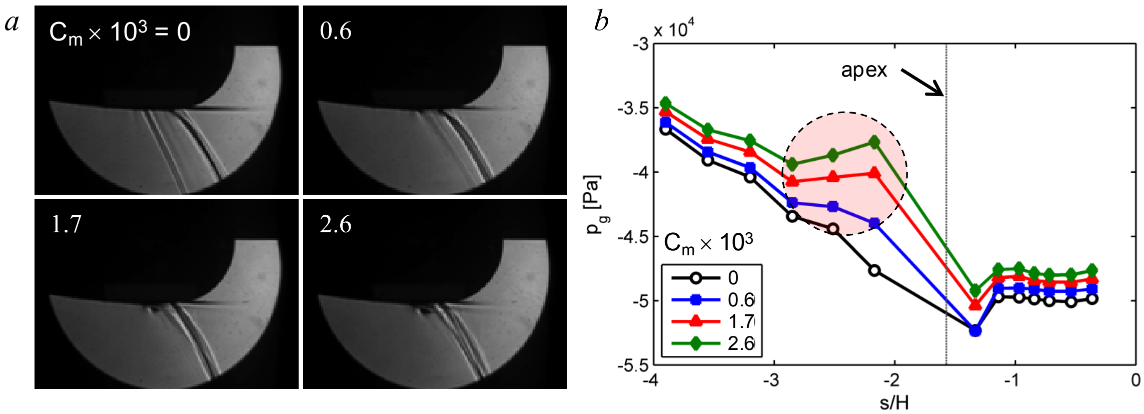

Figure 13. *Shock control in the choked flow at four C_m: a) Schlieren visualization and b) surface static pressure profiles.*

Consequently, it is expected that there is no significant difference in the acoustic spectra either, when the controlled flows are compared in the pre-choked and choked regimes. The acoustic spectra corresponding to the cases shown in Figure 13 are shown in Figure 14. Baseline flow spectrum (C_m = 0) indicates a presence of two broad dominant frequencies f_3 and f_4. Similar to the control effect in the pre-choked regime, there is, to a lesser extent, a reduction in energy of acoustic fluctuations over low frequencies, and some increase over the higher frequency range. Also, no full suppression of dominant frequencies is measured under the flow control, and only minor differences among the three controlled cases are observed, just as in the case of the pre-choked regime.

The second flow control approach is focused on control of the shock-induced flow separation, rather than directly on the source of separation – a transonic shock. Therefore, the same fluidic oscillating jet array used in the shock control was repositioned just downstream from the ramp profile apex, i.e., just downstream from the shock origination. The resulting flow effects are tested for the four $C_m \times 10^3$ = 0.6, 1.7, 2.8, and 4.0. Similar to the shock-control approach, both pre-choked and choked flow regimes are studied.

Figure 15 shows the static pressure profiles and schlieren visualization images for the baseline and controlled pre-choked (M = 0.59) flow regime. The appearance and major characteristics of the baseline shock are the same as seen in Figure 11 (as they should not depend on the particular flow control insert). There are several important features to be noted with respect to the controlled-flow pressure profiles. First, opposite to the shock-controlled approach, there is very little effect on the global flow upstream from the apex – it can be argued that there is a slight increase in the losses for the low jet flow rates, which is then reversed for the highest control flow rate. Second, as the flow rates increase, there is a clear shift in the separation point of the flow, i.e., the higher flow control rates induce a delay in the flow separation off the aft cylinder. The resulting effect on the shear layer can be surmised from the accompanying schlieren images: as the control jets are activated, suppression of the shear layer sharp density gradients increases with the jets' flow rate, up to the point that no sharp density gradients are detected behind the shock for the highest flow rate (C_m = 0.004). Although this control approach does not target the shock directly, it is seen that some indirect effect on the shock is induced, as the shock origin shifts slightly downstream with flow control, and its width appears to widen as well. Overall, it is argued that the main effect of the flow control in this case is in the enhanced mixing and spreading of the shear layer at lower flow rates, while the control effect is seen as a combination of the flow separation delay and enhanced mixing and spreading of the shear layer at the higher flow rates.

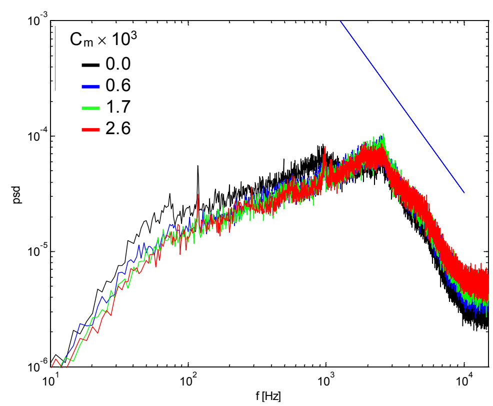

Figure 14. *Power spectra of the sound pressure for the baseline (C_m = 0) and controlled flows with varying C_m for the flow conditions equivalent to Fig. 13.*

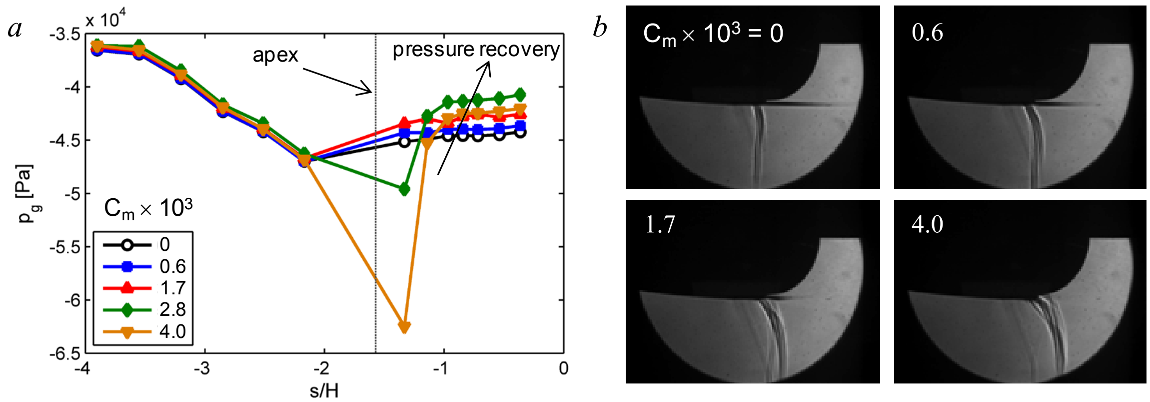

Figure 15. *Separation control in the pre-choked flow (M = 0.59) at four C_m: a) surface static pressure profiles and b) Schlieren visualization.*

Figure 16 shows the mean flow fields for the baseline flow and the controlled flows that correspond to schlieren images shown in Figure 15b. The baseline flow (Figure 16a) exhibits a typical vorticity signature of shear layer formation and evolution, where sharp velocity gradients of the boundary to shear layer slowly diffuse downstream as the initially narrow shear layer grows by entrainment. Besides the mild vectoring of the shear layer for the weakest control C_m = 0.0006 (Figure 16b), a more rapid spreading of the shear layer is observed in diffused vorticity concentrations, which is attributed primary to the mixing effect of the control jets. Just like in schlieren visualization, further increase in C_m (Figure 16c) induces more pronounced vectoring of the shear layer and rapid mixing with the surrounding air, which results in significantly diffused levels of vorticity. Some local flow reattachment to Coanda surface is also seen in the averaged flow field. Finally, as the highest C_m (Figure 16d), further diffusion of the shear layer vorticity is accompanied by separation delay, but also with a 'buckling' of the shear layer off the surface. This buckling effect is attributed to the coupled dynamics of the delayed flow separation and the shock, which, under the altered pressure field, also advances downstream, past the actuators (see the corresponding schlieren image in Figure 15b).

Figure 17 shows the acoustic spectra for the cases corresponding to those discussed in Figure 15. First, just as in the case of the upstream control spectra in the pre-choked flow (Figure 12), spectral peaks at f_1, f_2, and f_3 are still present in the baseline flow. Once the control jets are activated, there is a clear shift

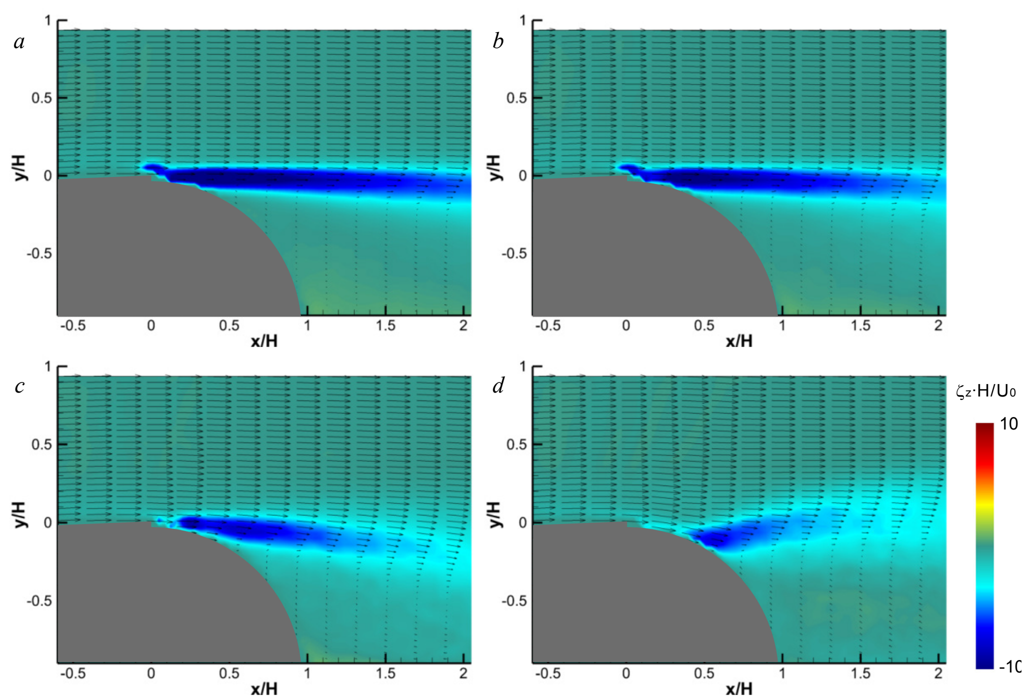

Figure 16. *Raster plot of the mean vorticity ζ_z for the baseline flows at M = 0.59 (a) and the controlled flows at $C_m \times 10^3$ = 0.6 (b), 1.7 (c), and 4.0 (d).*

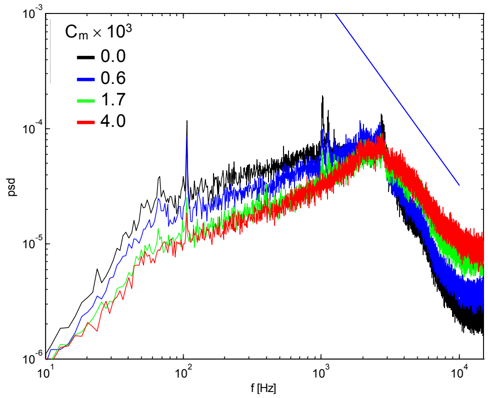

Figure 17. *Power spectra of the sound pressure for the baseline (C_m = 0) and controlled flows with varying C_m for the flow conditions equivalent to Fig. 15.*

with respect to the baseline case, where energy of sound pressure decreases for low frequencies, up to about 2 kHz, and there is a trend of increased suppression with the control C_m. Similar to the upstream control (Figure 12), energy of the high frequency fluctuations increases with an increase in C_m, and both the low-frequency decrease and high-frequency increase are more pronounced in the separation control measurements shown in Figure 17, when compared to the shock-controlled approach in Figure 12. It should be also emphasized that, up to the highest C_m = 0.004, the control effect does not seem to completely suppress any of the significant frequencies in the spectra, but both f_1 and f_3 become completely suppressed for the highest control flow rate. As the accompanying schlieren visualization for this case (Figure 15b) indicates that the shear layer sharp density gradient becomes fully suppressed at C_m = 0.004, this finding further supports conclusion that the low characteristic frequencies f_1 and f_3, which are of the order of 1 kHz, are related to the shear layer dominant frequencies.

The corresponding cases of the shear layer control in the choked flow regime are shown in Figure 18 in the same manner as in Figure 15 for the pre-choked flow, keeping the absolute control flow rates the same as in the pre-choked regime. The pressure profiles (Figure 18a) show characteristic invariant pressure distribution of the choked flow upstream from the shock. Once the flow control is activated, two major alterations of the flow filed are detected. First, there is a separation delay that increases progressively with C_m (Figure 18a), down almost to s/H = -1 for the highest C_m. Second, the shlieren visualization indicates progressive diffusion of sharp density gradients with an increase in C_m, virtually completely suppressing the sharp shear layer signature at the highest flow rate. Overall, the resulting effects in the choked regime are similar to those of the pre-choked counterpart, and it is seen in this control approach again that the control tool is robust enough to diminish sharp density gradients behind the shock.

Figure 19 shows the mean flows fields that correspond to the flow conditions visualized in Figure 18b. Similarly to the pre-choked controlled flows, increasing C_m induces more pronounced downward vectoring of the shear layer accompanied by the more diffused vorticity levels. These are an indication of the jets' mixing effect aided with separation delay for the highest C_m (Figure 19d). No shear layer 'buckling' is observed in these cases, although it is possible that the further increase in C_m would impose such an effect (not the higher C_m in Figure 16d).

Power spectra of the baseline and controlled flows under the choked regime are shown in Figure 20 for the cases presented in Figure 18. The baseline flow exhibits two signature broadband spectral peaks at f_3 and f_4. The effects of the control jets are analogous to their pre-choked counterparts (Figure 17): broadband reduction of the low frequency, and increase in the high-frequency energy content, accompanied with a full suppression of the shear layer

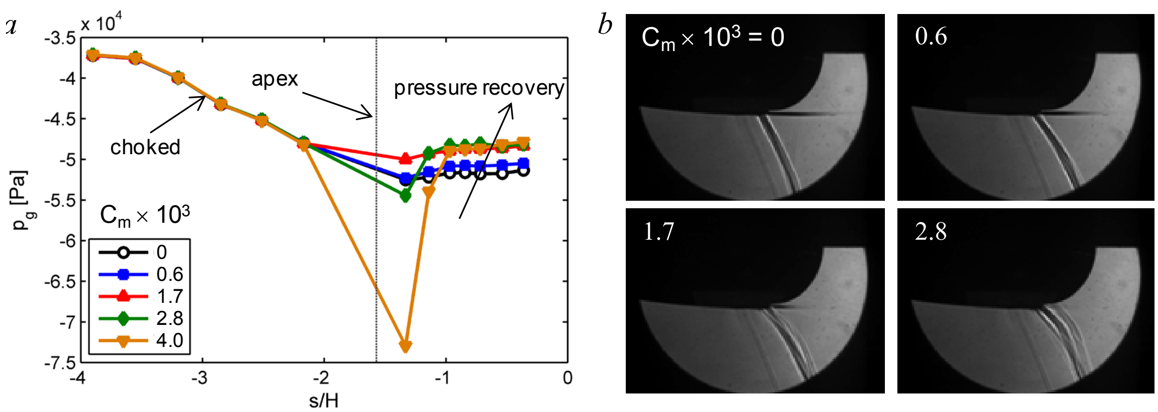

Figure 18. *Separation control in the choked flow at four C_m: a) surface static pressure profiles and b) Schlieren visualization.*

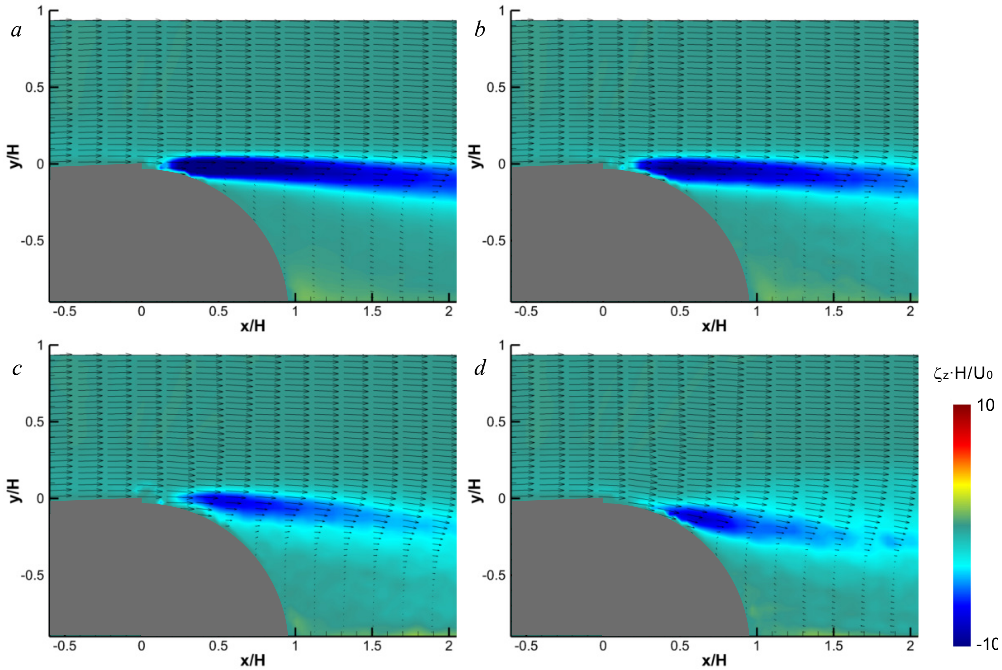

Figure 19. *Raster plot of the mean vorticity ζ_z for the baseline choked flow (a) and the controlled flows at C_m = 0.6 (b), 1.7 (c), and 2.8 (d).*

attributed peak at f_3. Presumably due to the broadband nature of this spectral peak, not only the highest control flow rate, but also the middle one (C_m = 0.0017) was sufficient to fully suppress the spectral peak at f_3 (~ 1 kHz).

Besides a nominal cylindrical aft surface profile, an alternate surface geometry profile is also tested, having a lower curvature (see Figure 3b), which is partially motivated by assumption that any scaled-up (prototype) geometry would inherently have a reduced surface curvature compared to its scaled-down model. Two resulting baseline flows are represented in Figure 21 for the pre-choked and choked flow regimes. The shocks appear at approximately the same locations as in the cylindrical profile (Figure 5), but two main differences are noted: the resulting shear layer appears weaker in terms of the density gradient and its persistence downstream from its origination, and the second one, not visible in a still image, that the normal shock's oscillation range increases with reduction of the surface curvature. The former observed difference can be attributed to reduction of the nearly-stagnant flow region below the incipient shear layer, which suppresses entrainment and its resulting growth. The latter effect is believed to be related to the changed surface pressure gradient, which relaxes the flow separation condition over larger spatial extent. This ad-hoc test indicates that stronger attention should be paid to influence of the surface curvature to the resulting aerodynamic properties of the shock-induced separation and its ensuing flow field, and warrants further investigation.

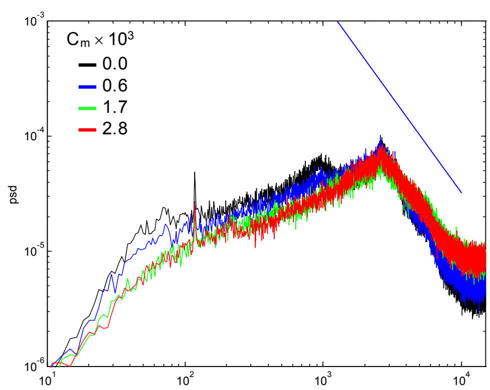

Figure 20. *Power spectra of the sound pressure for the baseline (C_m = 0) and controlled flows with varying C_m for the flow conditions equivalent to Fig. 18.*

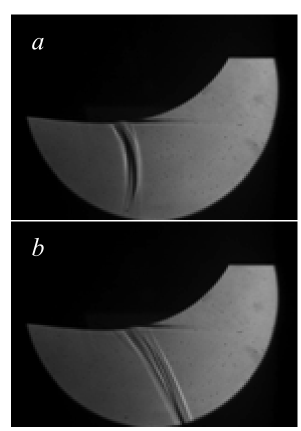

Figure 21. *Schlieren images of the pre-choked (a) and choked (b) flow shock-induced separation over a reduced surface curvature.*

V. Conclusions

The present experimental investigation explores the feasibility of different active flow control approaches in suppression of 'large scale' unsteadiness downstream of shock-induced flow separation over a rounded ramp in a transonic flow regime. The transonic shock forms over the cylindrical aft surface of the ramp, over which a nominally subsonic upstream flow compresses up to the formation of a normal shock downstream from the ramp apex. The aerodynamic aspects of both baseline and controlled flows are characterized over such a nominal geometry.

Preliminary study of the test section flows under all realizable tunnel speeds established the two shock-related flow regimes – pre-choked and choked, for the test geometry. As the oncoming Mach number is increased, a localized normal shock forms downstream from the ramp apex. This local shock gains in strength and spatial extent off the surface with further increase in M, up to the point when it spans the full test section height. After that point, the tunnel flow becomes choked, there is no change in the mass flow rate through the tunnel, and a further increase in the blower suction only lowers the back pressure. In response, nominally normal shock tilts in the choked regime to accommodate altered back pressure, along with its slight downstream displacement. Although it can be argued that the pre-choked regime would be more relevant for any external airborne application, the current study considers both pre-choked and choked flow regimes for any given flow control approach in order to test the robustness of the control tool, while keeping the pre-choked regime of primary interest.

Analysis of the acoustic signal measured by the microphone underneath the incipient shear layer isolated several characteristic acoustic frequencies as the flow over the ramp is driven from subsonic to the pre-choked, and to the choked states. The acoustic oscillations prior to the shock formation indicate multiple peaks between f_1 (~ 1 kHz)and f_2 (~ 2.5 kHz). As the tunnel speed is increased and the pressure/density fluctuations increase upstream from the ramp apex, f_2 becomes stronger and dominates the spectrum. However, along with the appearance and strengthening of the normal shock in the pre-choked regime, both f_1 and f_2 become largely suppressed and broadened. In addition, once the flow transitions into the choked regime, two broad but distinguished peaks at f_3 and f_4 are re-established. Simultaneous analysis of the corresponding schlieren visualization shows that as the shock is formed in the pre-choked regime both f_1 and f_2 exhibit discontinuous change in slope along with significant suppression of the energy of each peak. This discontinuous drop is more pronounced for the dominant frequency f_1, which could be related to the boundary layer thickening at the shock formation, which would in turn lower the shear layer dominant frequency. Therefore, it is possible that the first dominant frequency is related to the dominant shear layer frequency. The second dominant frequency f_2 becomes significantly amplified at the point of formation of strong pressure/density fluctuations associated with the initial compression waves as precursors to the shock formation, but it is afterwards suppressed and broadened just like f_1, once the shock is fully established. This frequency therefore could be associated with the dynamics of the coalescing compression waves. It is interesting to note that the flow in the fully established pre-choked regime does not exhibit any sharp acoustic features, which may also point to the shock oscillation decoupling from the shear layer dominant frequencies, and variations in shock oscillation across the test span, possibly further accentuated by the end-wall effects.

Two main flow control approaches are tested with respect to suppression of 'large-scale' flow unsteadiness: active pre-shocking of the flow upstream from the main shock and suppression of strong velocity/density gradients in the shear layer upon incipient flow separation. The former builds on a well-known passive pre-shocking of the flow, typically in supersonic regimes, and thereby weakening of the primary shock. It is proposed that an active flow control source is utilized instead of typical passive surface 'obstacles' that are used in the supersonic flows. The latter approach is motivated by placing the control focus on the resulting shock-induced separation and its mitigation, rather than direct control of its source – a normal shock. Both control approaches utilize active control components – fluidic oscillating jets that combine nonzero net mass injection into the flow with high-frequency vorticity generation.

Surface pressure profiles upon the onset of upstream flow control indicate that there is a pressure increase upstream from the apex (shock) due to the flow control jets interaction with the oncoming flow, which virtually shapes an 'apparent flow boundary'. As a consequence, the outer flow becomes locally slowed down just upstream from the shock formation, which contributes to its weakening. In addition, once the control jets are activated, there is a clear shift in acoustic energy across the scales, where energy of sound pressure decreases for low frequencies, up to about 1 kHz, and energy of high-frequency acoustic oscillations increases somewhat proportionally with the jets' flow rate. Presumably the most interesting consequence of the flow control is manifested in suppressed sharp density gradients in the shear layer observed with schlieren visualization, proportional to the jets' mass coefficient. This suppression of sharp velocity/density gradients is attributed to the enhanced mixing of the downstream flow. Contrary to the first flow control approach, the second approach that targets the shear layer shows there is a clear shift in the separation point of the flow with the jets' mass coefficient. The accompanying schlieren images indicate, similar to the first control approach, that suppression of the shear layers' sharp density gradients increases with the jets' flow rate, up to the point that no sharp density gradients are detected behind the shock for the highest flow rate ($C_m = 0.004$). Although the second control approach does not target the shock directly, the shock origin shifts slightly downstream with flow control, and its width appears to widen as well. Overall, it is argued that the main effect of the flow control in this case is seen as a combination of the enhanced mixing and spreading of the shear layer, assisted by the flow separation delay at the higher flow rates.

Acknowledgment

The authors would also like to acknowledge the Air Force Research Laboratory funding for this work, as well as support by Michael Paul and Donald J. Wittich.

References

[1]Pearcey, H.H., "Shock-Induced separation and its prevention by design and boundary layer control. Boundary Layer and Flow control Vol. 2. 1961

[2]Delery, J.M., "Shock Wave/Turbulent Boundary Layer Interaction and its Control," *Prog. Aerospace Sci*., Vol. 22, 1985, pp. 209-280.

[3]Viswanath, P.R., "Shock-Wave-Turbulent-Boundary-Layer Interaction and its Control: A Survey of Recent Developments," *Sadhana*, Feb., 1988, pp. 45-104.

[4]Bushnell, D. M., "Shock Wave Drag Reduction," *Annual Review of Fluid Mechanics*, Vol. 36, 2004, pp. 81-96.

[5]Ferri A., "Experimental Results with Airfoils Tested in the High-Speed Tunnel at Guidonia", *Atti. Di Godonia*, No. 17, 1939, Eng. Trans. 1940.

[6]Liepmann, H.W., "Interaction between boundary layer and shock waves in transonic flow," *Journal of Aeronautical Sciences,* Vol. 13, 1946, pp. 623-637.

[7]Ackeret, J., Feldmann, F., and Rott, K., "Investigations of Cornpression Shocks and Boundary Layers in Gases Moving at High Speed," NACA TM 1113, 1947.

[8]Liepmann, H.W.; Roshko, A.; and Dhawan, S., "On reflection of shock waves from boundary layers," *National Advisory Committee for Aeronautics*, Report 1100, 1951, pp. 889-917.

[9]Adamson, T.C. Jr. and Messiter, A.F., "Analysis of Two-Dimensional Interactions Between Shock Waves and Boundary Layers," *Annual Review of Fluid Mechanics*, Vol. 12, 1980, pp. 103-138.

[10]Andreopoulos, J. and Muck, K.-C., "Some New Aspects of the Shock-Wave/Boundary-Layer Interaction in Compression-Ramp Flows," Journal of Fluid Mechanics, Vol. 180, 1987, pp. 405-428.

[11]Dolling, D.S., "Fifty Years of Shock-Wave/Boundary-Layer Interaction Research: What Next?," *AIAA Journal*, Vol. 39, No. 8, 2001, pp. 1517-1531.

[12]Lin, J.C., "Review of research on low-profile vortex generators to control boundary-layer separation," *Progress in Aerospace Sciences*, Vol. 38, 2002, pp. 389-420.

[13]Ashill, P.R., Fulker, J.L., and Hackett, K.C., "Research at DERA on Sub Boundary Layer Vortex Generators (SBVGs)," AIAA Paper 2001-0887, Jan, 2001.

[14]Barter, J.W., Dolling, D.S., "Experimental Study of the Use of Vortex Generators to Reduce Fluctuating Pressure Loads in Shock Wave Turbulent Boundary Layer Interactions." AIAA Paper 1993-4335, Oct, 1993.

[15]Stanewsky, E. (Editor). "Drag Reduction by Shock and Boundary Layer Control: Results of the project EUROSHOCK II. Jun 20, 2002.

[16]Holden, H. and Babinsky, H., "Effect of Microvortex Generators on Separated Normal Shock/Boundary Layer Interactions," *Journal of Aircraft*, Vol. 44, No.1, 2007, pp. 170-174.

[17]Lee, S., Loth, E., and Babinsky, H., "Normal Shock Boundary Layer Control with Various Vortex Generator Geometries," *Computers and Fluids*, Vol. 49, 2011, pp. 233-246.

[18]Krogmann, P., Stanewsky, E., and Thiede, P., "Effects of Suction on Shock/Boundary-Layer Interaction and Shock-Induced Separation," *Journal of Aircraft*, Vol. 22, No.1, 1985, pp. 37-42.

[19]Souverein, L.J. and Debieve, J.-F., "Effect of Air Jet Vortex Generators on a Shock Wave Boundary Layer Interaction," *Experiments in Fluids*, Vol. 49, 2010, pp. 1053-1064.

[20]Kalra, C.S, Shneider, M.N., and Miles, R.B., "Numerical Study of Boundary Layer Separation Control Using Magnetogasdynamic Plasma Actuators," *Physics of Fluids*, Vol. 21, 2009, 106101.

[21]Kalra, C.S, Zaidi, S.H., Miles, R.B., and Macheret, S.O., "Shockwave–Turbulent Boundary Layer Interaction Control Using Magnetically Driven Surface Discharges," *Experiments in Fluids*, Vol. 50, 2011, 547-559.

[22]Narayanaswamy, V., Clemens, N.T., and Raja, L.L., "Investigation of a Pulsed-Plasma Jet for Shock / Boundary Layer Control," AIAA Paper 2010-1089, Jan, 2010.